A&A 647, L1 (2021)
https://doi.org/10.1051/0004-6361/202140400

Astronomy & Astrophysics

LETTER TO THE EDITOR

Starspot modelling of the TESS light curve of CVSO 30

C. Koen

Department of Statistics, University of the Western Cape, Private Bag X17, Bellville 7535, Cape, South Africa
e-mail: ckoen@uwc.ac.za

Received 22 January 2021 / Accepted 22 February 2021

ABSTRACT

Aims. I aim to investigate whether the photometric variability in the candidate host star CVSO 30 can be explained by starspots.
Methods. The Transiting Exoplanet Survey Satellite (TESS) light curve of CVSO 30 is separated into two independent non-sinusoidal periodic components. A starspot modelling technique is applied to each of these components.
Results. Combined, the two model light curves reproduce the TESS observations to a high accuracy, obviating the need to invoke planetary transits to describe part of the variability.

Key words. stars: variables: T Tauri, Herbig Ae/Be

1. Introduction

The T Tauri star CVSO 30 was discovered by Briceño et al. (2005). Van Eyken et al. (2012) analysed extensive Palomar Transit Factory observations of the star and found periodic low-amplitude depressions in the light curve with durations of ∼2 h. These were ascribed to planetary transits. A second planetary candidate (CVSO 30c), found by direct imaging, was announced by Schmidt et al. (2016) (but see Lee & Chiang 2018, for a different interpretation). The possible association of planets with CVSO 30 is of particular interest due to the young age of the star (∼2.6 Myr; Briceño et al. 2005). Other authors who have obtained further observations of periodic flux dips, or who proposed detailed models for these, include Raetz et al. (2016), Barnes et al. (2013), Kamiaka et al. (2015), Yu et al. (2015), Koen (2015), Howarth (2016), Onitsuka et al. (2017), and Tanimoto et al. (2020).

Koen (2015) pointed out that the periodic flux dips discovered by Van Eyken et al. (2012) may simply be part of a complex variation pattern of the star. This theme was elaborated on by Koen (2020) and Bouma et al. (2020), who independently came to the conclusion that the star was a binary T Tauri with no overt planetary companions. The light variations of both stars are thought be complex, showing dips. This Letter confirms that finding and presents models for both sets of variations.

A variety of explanations for complex light curves in young late-type stars have been discussed in the literature, for example in Stauffer et al. (2017, 2018), Zhan et al. (2019), and Günther et al. (2020). Here, it is shown that the variations could be due to dark features on the surfaces of the stars. The modelling methodology is very similar to that in Koen (2021).

2. The starspot model

The fundamental equations describing the flux variations due to the rotation of a spotted star are

$$I(\psi) = \left[\int_{\text{all}} F_* h(\mu)\mu \,\mathrm{d}S - \int_{\text{spots}} (F_* - F_\mathrm{s}) h(\mu)\mu \,\mathrm{d}S\right]$$

$$I_0 = \int_{\text{all}} F_* h(\mu)\mu \,\mathrm{d}S = \pi(c_0 + 2c_1/3 + c_2/2)F_*$$

$$h(\mu) = c_0 + c_1\mu + c_2\mu^2, \tag{1}$$

where: ψ is the rotational phase; $I(\psi)$ and I_0 are, respectively, the observed luminosity and the luminosity that would have been observed from an unspotted stellar surface; F_* and F_s are, respectively, the fluxes from unspotted and spotted surface areas; the function $h(\mu)$ describes limb darkening; and $\mu = \cos\gamma$, where γ is the angle between the surface normal and the line of sight towards the observer (see e.g., Dorren 1987, and references therein). Equation (1) is a slight generalisation of Eq. (1) in Koen (2021) to quadratic, rather than linear, limb darkening; regarding the usual coefficients a and b (e.g., Claret 2017),

$$c_0 = 1 - a - b \quad c_1 = a + 2b \quad c_2 = -b.$$

It follows from this Letter's Eq. (1) that

$$I(\psi)/I_0 \approx 1 - \int_{\text{spots}} (1 - F_\mathrm{s}/F_*) h(\mu)\mu \,\mathrm{d}S \Big/ [\pi(c_0 + 2c_1/3 + c_2/2)]. \tag{2}$$

Koen (2021) showed that by discretising the integral, Eq. (2) can be approximated by the linear regression equation

$$\boldsymbol{y} = \mathbf{G}\boldsymbol{z} + \boldsymbol{e}. \tag{3}$$

In Eq. (3), $\boldsymbol{y}$ is a column vector with elements

$$y_\ell = [I_0 - I(\psi_\ell)]/I_0 \quad \ell = 1, 2, \ldots, L.$$

Each entry in the vector $\boldsymbol{z}$ corresponds to a particular small surface element:

$$z_j = 1 - F_\mathrm{s}(j)/F_* \quad j = 1, 2, \ldots, p, \tag{4}$$

that is, $z_j = 0$ if pixel j is unspotted. Entries in the $L \times p$ matrix $\mathbf{G}$ depend only on the limb darkening coefficients and on the angle γ_j between the local surface normal and the line of sight. The vector $\boldsymbol{e}$ models noise.

Constraints need to be placed on $\boldsymbol{z}$ in order to make the regression problem tractable. Using the notation

$$\|z\|_n \equiv \left[\sum_j |z_j|^n\right]^{1/n}$$

for the norm-n of $\boldsymbol{z}$, a simple constrained form of Eq. (3) is

$$\min_z \left[\frac{1}{2}\|\boldsymbol{y} - \mathbf{G}\boldsymbol{z}\|_2^2 + \lambda\|z\|_n\right], \tag{5}$$

where the constant λ determines the relative importance of the model fit and the parsimony of the non-zero components of $\boldsymbol{z}$. The cases $n = 1$ and $n = 2$ are known, respectively, as 'lasso' and 'ridge' regression in the literature (e.g., Hastie et al. 2009). Both lasso and ridge regression favour small values of z_j (i.e. small deviations from the undisturbed photospheric flux). In the case of lasso regression, a premium is placed on zero values, that is, the regression can be seen as providing an optimally parsimonious model with a minimum number of pixels that have depressed fluxes. The quadratic programming problem (5) can easily be solved using software such as CVX (e.g., Grant & Boyd 2020).

A standard regression goodness of fit statistic is the 'coefficient of determination',

$$R^2 = 1 - \sum_\ell \epsilon^2(\psi_\ell) \Big/ \sum_\ell [m(\psi_\ell) - \overline{m}]^2 ,$$

where

$$\epsilon(\psi) = m(\psi) - \widehat{m}(\psi),$$

$m(\psi)$ and $\widehat{m}(\psi)$ being, respectively, the observed and the predicted magnitudes at phase ψ. Here, R^2 measures the fraction of the observed variability of m explained by the model. In addition to R^2, which is not very sensitive to locally poor fits, two other useful statistics are

$$d = \max_\ell |\epsilon(\psi_\ell)|$$

$$\sigma_\epsilon = \left[\frac{1}{L}\sum_\ell \epsilon^2(\psi_\ell)\right]^{1/2} . \tag{6}$$

Values of d and σ_ϵ will be given as percentages of the peak-to-peak observed magnitudes in what follows.

Because of the particular formulation of the problem, only two physical quantities (the inclination angle and limb darkening) need to be specified. Results are not very sensitive to the inclination angle i; a few different values were tried, and those giving the smallest prediction errors were adopted. If it is assumed that the two stars making up the binary system are fairly similar, with $T_{\rm eff} \approx 3400$ K (Briceño et al. 2019; Koen 2020) and $\log g = 4.5$, then typical limb darkening coefficients for the Transiting Exoplanet Survey Satellite (TESS) filter are $a = 0.18$, $b = 0.44$ (Claret 2017).

Clearly, for dark starspots, $0 \le z_j \le 1$ for all j. The upper limit can be sharpened by noting that for a stellar temperature ~3400 K, starspot temperatures will generally be about 400 K lower (see Fig. 7 in Berdyugina 2005). Assuming blackbody radiation and using the TESS filter transmission function[1], $F_s/F_* \ge 0.49$ or $z_j = 1 - F_s/F_* \le 0.51$.

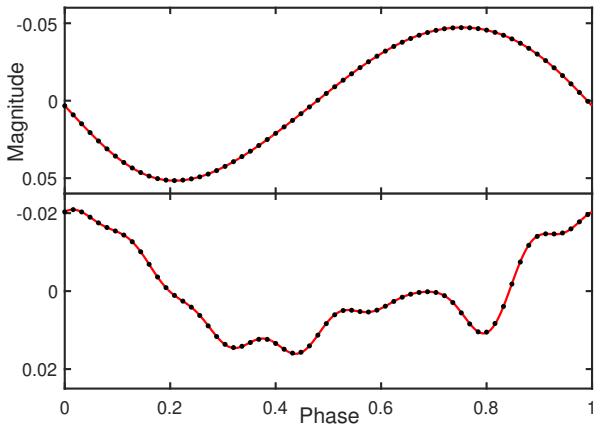

Fig. 1. Norm-1 model fits (dots) to the phased TESS light curves of the two components of CVSO 30 (solid lines). *Top panel*: 0.4991 d periodicity. *Bottom panel*: 0.4486 d periodicity.

Table 1. Details of the spot models.

Star	Norm	λ	i (deg)	f	σ_ϵ	d
1	1	1E−7	60	0.05	0.045	0.133
	2	1E−4	60	0.48	0.165	0.309
2	1	1E−9	70	0.37	0.264	0.790
	2	1E−7	70	0.66	0.243	0.648

Notes. Peak-to-peak amplitudes are 0.099 and 0.037 mag for stars 1 and 2, respectively. The 'filling factor' f is the fraction of the 20 000 coefficients z_j that are larger than 0.01 (i.e. notably non-zero). The statistics $\sigma_{\rm p}$ and d are defined in Eq. (6) and are given as percentages of the peak-to-peak amplitudes.

One mathematical constant, λ, must be specified. This parameter controls the tradeoff between the goodness of fit of the model and the number of surface elements with $F_s \ne F_*$ required to achieve the fit. The largest values that still gave excellent global fits ($R^2 = 1$) were chosen. The surface of each star was subdivided into $p = 20\,000$ elements of equal area (2.06 deg^2).

3. Results

TESS (Ricker et al. 2015) observed CVSO 30 for 21.8 d at a two-minute cadence. The data are available from the Mikulski Archive for Space Telescopes (MAST) portal[2]. Koen (2020) and Bouma et al. (2020) argue that the light curve is the sum of contributions from two different stars. Because they are periodic, Fourier methods make short work of separating the two individual light curves. The larger amplitude variation has a base frequency of 2.0038 d^{-1} (period 0.49905 d), with at least two harmonics also evident in a periodogram of the observations. The second light curve is much more complex, showing power up to the seventh harmonic of the fundamental frequency 2.2292 d^{-1} (period 0.44859 d).

The two light curves are plotted in Fig. 1 (solid lines). The figure also shows norm-1 model fits (dots), which are indistinguishable from the observations on the scales of the diagram. Details of the two models are listed in Table 1, which also gives

[1] See e.g., https://heasarc.gsfc.nasa.gov/docs/tess/the-tess-space-telescope.html#bandpass

[2] https://mast.stsci.edu/portal/Mashup/Clients/Mast/Portal.html

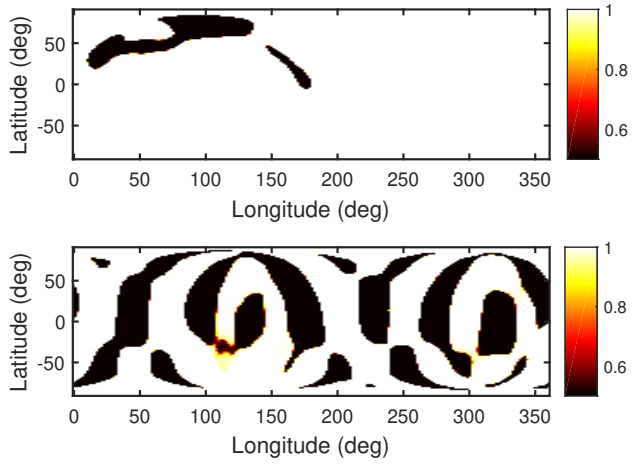

Fig. 2. Spot configurations giving rise to the model light curves in Fig. 1 (see Table 1 for further details). The colour coding indicates the ratio of local flux to the unspotted photospheric flux, i.e. it equals zero (one) for a completely dark (unspotted) area.

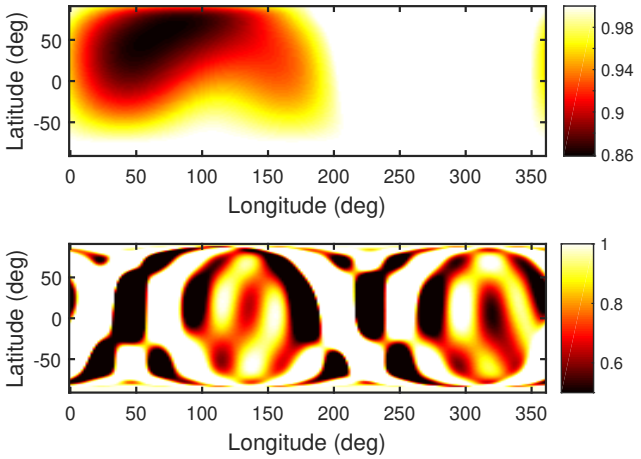

Fig. 3. Same as for Fig. 2, but for norm-2 models. The different intensity scales in the two panels should be noted.

parameters for norm-2 models. Spot patterns can be seen in Figs. 2 and 3.

A comparison of the combined model light curves and the TESS observations is given in Fig. 4. It is clear that the overall description of the data is very good. The residuals are dominated by two short stretches of systematic deviations visible towards the ends of the second and the last panels of Fig. 4. If they are excluded (spans of ~0.15 and ~0.47 d, respectively), the largest peak in the residual amplitude spectrum has a height of 2.8 millimagnitudes (at a period ~7.4 d). This can most likely be ascribed to systematics in the TESS observations and/or typical T Tauri variability.

4. Conclusions

It should be noted that starspot models based on photometry through a single filter are not unique, as is made abundantly clear by comparing Figs. 2 and 3 (see also e.g., Vogt 1981; Basri & Shah 2020). Multi-filter light curves and time series spectroscopy will go some way towards ameliorating this problem.

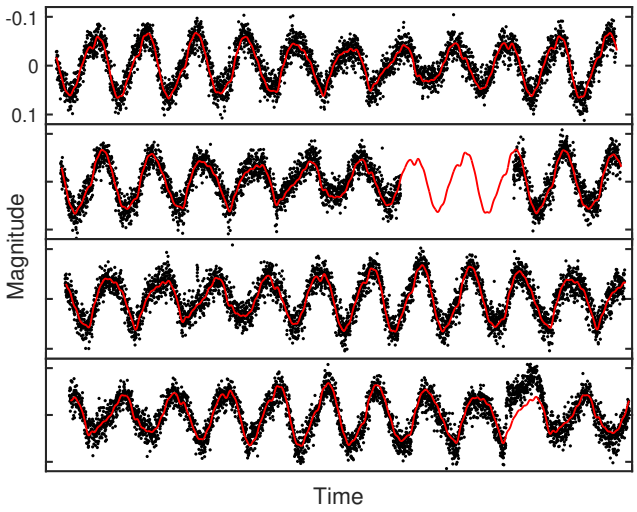

Fig. 4. Two-minute TESS measurements of CVSO 30 (shown with dots) and the sum of the two model light curves plotted in Fig. 1 (shown with the solid line). The width and height of each panel are 5.7 d and 0.24 mag, respectively. The total duration of the TESS run was 21.8 d.

Nonetheless, it has been demonstrated that starspot models have the potential to accurately reproduce the variability in CVSO 30 without invoking additional sources of variability, such as planetary transits.

Acknowledgements. The author appreciates greatly that the developers of the CVX package makes it freely available for academic use. The easy access to TESS photometry via the MAST portal is gratefully acknowledged.

References

Barnes, J. W., Van Eyken, J. C., Jackson, B. K., Ciardi, D. R., & Fortney, J. J. 2013, ApJ, 774, 53
Basri, G., & Shah, R. 2020, ApJ, 901, 14
Berdyugina, S. V. 2005, Liv. Rev. Sol. Phys., 2, 8
Bouma, L. G., Hartman, J. D., Brahm, R., et al. 2020, AJ, 160, 86
Briceño, C., Calvet, N., Hernández, J., et al. 2005, AJ, 129, 907
Briceño, C., Calvet, N., Hernández, J., et al. 2019, ApJ, 157, 85
Claret, A. 2017, A&A, 600, A30
Dorren, J. D. 1987, ApJ, 320, 756
Grant, M., & Boyd, S. 2020, The CVX User's Guide, http://cvxr.com/cvx
Günther, M. N., Berardo, D. A., Ducrot, E., et al. 2020, AAS J., submitted [arXiv:2008.11681]
Hastie, T., Tibshirani, R., & Friedman, J. 2009, The Elements of Statistical Learning, 2nd edn. (Berlin: Springer-Verlag)
Howarth, I. D. 2016, MNRAS, 457, 3769
Kamiaka, S., Masuda, K., Xue, Y., et al. 2015, PASJ, 67, 94
Koen, C. 2015, MNRAS, 450, 3991
Koen, C. 2020, MNRAS, 494, 4349
Koen, C. 2021, MNRAS, 500, 1366
Lee, C.-H., & Chiang, P.-S. 2018, ApJ, 852, L24
Onitsuka, M., Fukui, A., Narita, N., et al. 2017, PASJ, 69, L2
Raetz, St., Schmidt, T. O. B., Czesla, S., et al. 2016, MNRAS, 460, 2834
Ricker, G. R., Winn, J. N., Vanderspek, R., et al. 2015, J. Astron. Telesc. Instrum. Syst., 1, 014003
Schmidt, T. O. B., Neuhäuser, R., Briceño, C., et al. 2016, A&A, 593, A75
Stauffer, J., Collier-Cameron, A., Jardine, M., et al. 2017, AJ, 153, 152
Stauffer, J., Rebull, L., David, T., et al. 2018, AJ, 155, 63
Tanimoto, Y., Yamashita, T., Ui, T., et al. 2020, PASJ, 72, psz145
Van Eyken, J. C., Ciardi, D. R., von Braun, K., et al. 2012, ApJ, 755, 42
Vogt, S. S. 1981, ApJ, 250, 327
Yu, L., Winn, J. N., Gillon, M., et al. 2015, ApJ, 812, 48
Zhan, Z., Günther, M. N., Rappaport, S., et al. 2019, ApJ, 876, 127